

Role of Fe intercalation on the electronic correlation in resistively switchable antiferromagnet Fe_xNbS_2

Wenxin Li,¹ Jonathan T. Reichanadter,^{2,3,4} Shan Wu,^{3,4,5} Ji Seop Oh,^{3,6,7,8} Rourav Basak,⁹ Shannon C. Haley,³ Siqi Wang,¹ Joshua E. Chaparro Mata,¹ Elio Vescovo,¹⁰ Donghui Lu,¹¹ Makoto Hashimoto,¹¹ Christoph Klewe,¹² Suchismita Sarker,¹³ Jessica L. McChesney,¹⁴ Alex Frañó,⁹ James G. Analytis,^{3,15} Robert J. Birgeneau,^{3,4} Jeffrey B. Neaton,^{3,4} and Yu He^{1,*}

¹*Department of Applied Physics, Yale University, New Haven, Connecticut 06511, USA*

²*Department of Electrical Engineering, University of California Berkeley, California, 94720, USA*

³*Department of Physics, University of California Berkeley, California, 94720, USA*

⁴*Material Sciences Division, Lawrence Berkeley National Lab, Berkeley, California, 94720, USA*

⁵*Department of Physics, Santa Clara University, Santa Clara, CA, 95053*

⁶*Department of Physics and Astronomy, Rice University, Houston, Texas 77024, USA*

⁷*Department of Applied Physics, Sookmyung Women's University, Seoul 04310, Republic of Korea*

⁸*Institute of Advanced Materials and Systems, Sookmyung Women's University, Seoul 04310, Republic of Korea*

⁹*Department of Physics, University of California San Diego, California, 92093, USA*

¹⁰*National Synchrotron Light Source II, Brookhaven National Laboratory, Upton, New York 11973, USA*

¹¹*Stanford Synchrotron Radiation Lightsource, SLAC National Accelerator Laboratory, Menlo Park, California 94025, USA*

¹²*Advanced Light Source, Lawrence Berkeley National Laboratory, Berkeley, California 94720, USA*

¹³*Cornell High Energy Synchrotron Source, Cornell University, Ithaca, New York 14853, USA*

¹⁴*Advanced Photon Source, Argonne National Laboratory, Lemont, Illinois 60439, USA*

¹⁵*CIFAR Quantum Materials, CIFAR, Toronto, Ontario M5G 1M1, Canada*

(Dated: March 17, 2026)

Among the family of intercalated transition-metal dichalcogenides (TMDs), Fe_xNbS_2 is found to possess unique current-induced resistive switching behaviors, tunable antiferromagnetic states, and a commensurate charge order, all of which are tied to a critical Fe doping of $x_c = 1/3$. However, the electronic origin of such extreme stoichiometry sensitivities remains unclear. Combining angle-resolved photoemission spectroscopy (ARPES) with density functional theory (DFT) calculations, we identify and characterize a dramatic eV-scale electronic restructuring that occurs across the x_c . Moment-carrying Fe $3d_{z^2}$ electrons manifest as narrow bands within 200 meV of the Fermi level, distinct from other transition metal intercalated TMD magnets. These states strongly hybridize with itinerant electrons in TMD layer, rapidly lose coherence above x_c , and drive a transformation of the magnetic ground state via modification of the effective Fe-Fe exchange interaction. These observations resemble the exceptional electronic and magnetic sensitivity of strongly correlated systems upon charge doping, shedding light on the tunability of magnetic exchange interactions beyond nearest-neighbor and electronic correlation in magnetic TMDs.

Layered transition-metal dichalcogenides (TMD) TA_2 (T = Ta, Nb, Mo; A = Se, S) constitute a family of materials that are pivotal to modern condensed matter physics research, owing to their rich physical properties, ranging from charge density wave to superconductivity [1–4]. While most TMDs assume a weakly correlated non-magnetic ground state in their pristine phase [5, 6], their layered crystal structure often allows $3d$ transition metal intercalants to populate the van der Waals (vdW) gap (M_xTA_2 , M = $3d$ transition metal). This leads to a versatile class of tunable layered magnets that are often also highly metallic [7, 8], where indirect exchange via itinerant electrons is considered indispensable given the large M-site distances. Among all possible intercalant concentrations, materials with intercalation ratio $x_c = 1/3$, where the intercalated atoms typically form into a $\sqrt{3} \times \sqrt{3}$ superlattice [9] with non-centrosymmetric space group $P6_322$ and a folded Brillouin zone (Fig. 1 (a)), have drawn considerable interest with their extensive display of diverse magnetic

and electronic properties [10–18].

Figure 1 (c) tallies the Curie-Weiss temperature T_θ for different M_xTA_2 materials with highly tunable magnetic correlations [7, 16, 19–35]. Except for $\text{V}_{1/3}\text{NbS}_2$, which has a controversial magnetic ground state and was recently proposed as an altermagnet [37, 38], Fe intercalation is uniquely associated with both ferromagnetic ($T_\theta > 0$) and antiferromagnetic ($T_\theta < 0$) correlations depending on the atomic species of the TMD layers. This implies an active role of the TMD layer in mediating long-range Fe-Fe magnetic exchange, and makes Fe-intercalated TA_2 materials hosts for highly tunable magnetism and magnetoelectric transport properties. Recent neutron scattering and muon-spin relaxation (μSR) measurements reported two distinct magnetic phases across $x_c = 1/3$, i.e., the antiferromagnetic stripe order at $k_{m1} = (0.5, 0, 0)$ for $x < x_c$, and the antiferromagnetic zigzag order at $k_{m2} = (0.25, 0.5, 0)$ for $x > x_c$ [39, 40]. These nearly degenerate magnetic phases in Fe_xNbS_2 are sensitively

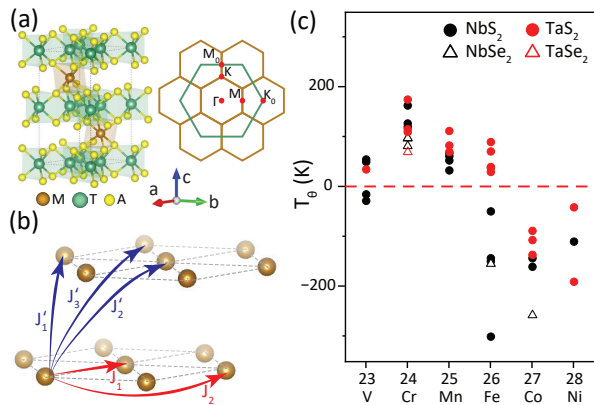


FIG. 1. Structural and magnetic property of intercalated TMD magnets. (a) The crystallographic structure and Brillouin zone of $3d$ metal intercalated TMDs M_xTA_2 with $x = 1/3$. Brown and Green hexagonal traces circumscribe the in-plane Brillouin zones for $M_{1/3}TA_2$ and TA_2 respectively. (b) Depiction of the Heisenberg exchange terms between in-plane and out-of-plane nearest, next-nearest, and third-nearest neighbor intercalant ions in M_xTA_2 . (c) Compilation of the Curie-Weiss temperatures for various M_xTA_2 systems with $x = 1/3$ [7, 16, 19–35].

decided by next-nearest-neighbor in-plane (J_2) versus out-of-plane (J'_2) exchange interactions [Fig. 1 (b)] [39] as identified from a Heisenberg Hamiltonian model [41], and are believed to cause its current-induced resistance switching property [42–44]. Moreover, a commensurate three-dimensional charge order, concomitant with the magnetic ordering, was recently discovered for $x > x_c$, signaling strongly coupled charge and magnetic degrees of freedom [45].

It remains a mystery why both the electrical transport and magnetic ordering properties experience a sudden change across $x_c = 1/3$ in and only in Fe_xNbS_2 . Previous electronic structure investigations in various intercalated TMD systems show that the low-energy electronic structure mainly derives from the TMD layers, while the charge doping and minor band hybridization effects come from the intercalated $3d$ transition metal [46–57]. While previous electronic structure studies on $Fe_{1/3}NbS_2$ [55] [56] and other TM-intercalated dichalcogenides (including but not limited to $Co_{1/3}NbS_2$ [48], $Cr_{1/3}NbS_2$ [50], $Ni_{1/3}NbS_2$ [53], $(Fe, Co)_{1/3}TaS_2$ [54] and $Fe_{1/3}NbSe_2$ [57]) identify emergent electronic states, the precise orbital link between these features and the intercalant species remains obscure. Crucially, the sensitivity of doping-controlled electronic and magnetic properties has not been explored, motivating systematic electronic and structural investigations into the exceptional electronics manifesting from Fe intercalants, especially whether and how low-energy itinerant electrons can affect the delicate indirect Fe-Fe exchange. In this work, we combine

angle-resolved photoemission spectroscopy (ARPES), X-ray photoelectron spectroscopy (XPS), single crystal X-ray diffraction (XRD), X-ray absorption spectroscopy (XAS) and density functional theory (DFT) calculations to investigate the electronic structure of Fe_xNbS_2 near the critical doping x_c , with a specific focus on the roles of itinerant and local electrons.

Given the extreme surface sensitivity of photoemission experiments [58, 59] and the existence of inhomogeneous surface termination in many intercalated TMD systems [51, 52], in particular, the putative surface termination effect in $Fe_{1/3}NbS_2$ reported in [55], micro-spot XPS measurements are performed on *in-situ* cleaved bulk sample surfaces to examine the iron homogeneity. Compared to the micron-scale inhomogeneity reported in $V_{1/3}NbS_2$ [52] and $Cr_{1/3}NbS_2$ [51], the surface iron inhomogeneity here can be constrained to less than 2.8% over similar length scales (see Fig. S2 in Supplementary Information (SI) [60]), enabling systematic electronic structure investigation as the bulk doping is tuned across $x_c = 1/3$. Figure 2 (a) shows the electronic structure measured with ARPES along Γ - K_0 from $x = 0.02$ to $x = 0.36$ (see Fig. S1 for spatial composition analysis [60]). For doping close to x_c , the $\sqrt{3} \times \sqrt{3}$ Fe-superlattice forms (Fig. S9 [60]) so that the M point of the Brillouin zone of $Fe_{1/3}NbS_2$ lies in the middle of Γ and K_0 points.

We first investigate the charge doping effect introduced by Fe intercalation. By tracking the energies of the band extrema for the Nb $4d$ and the S $3p$ bands, along with the Luttinger volume of the Nb $4d$ hole pockets around Γ and K [61] (see Fig. S7 for detailed procedures [60]), Fig. 2 (b) and (c) shows that Fe intercalants mediate substantial charge transfer at very dilute doping ($x = 0.02$) consistent with a rigid-band model [7, 46]. The Nb $4d$ and S $3p$ bands experience the same energy shift, indicating uniform electron doping to the TMD layer. Assuming full Fe ionization to Fe^{2+} [39], the charge transfer at $x = 0.02$ is larger than expected (gray dashed line in Fig. 2 (c)), which may be attributed to intrinsic tendency for excess Nb formation ($Nb_{1+\delta}S_2$) in the NbS_2 part of the sample [62] (see Fig. S1 and related discussion in SI [60]). Further iron intercalation causes this charge transfer process to reverse course, where the Nb $4d$ bands are gradually depleted (rising band bottom accompanied by a decreasing Luttinger volume), indicating potential electron localization at Fe sites. Only when doped to $x > x_c$, electrons move to fill Nb $4d$ bands again. On the other hand, S $3p$ bands shift toward higher binding energy with increasing Fe intercalation, affirming the presence of low-energy Fe state while increasing the global chemical potential. This shift of the S $3p$ bands further suggests reversed charge flow from Nb $4d$ states to Fe $3d$ states due to strong Fe-S bonds as the system approaches x_c .

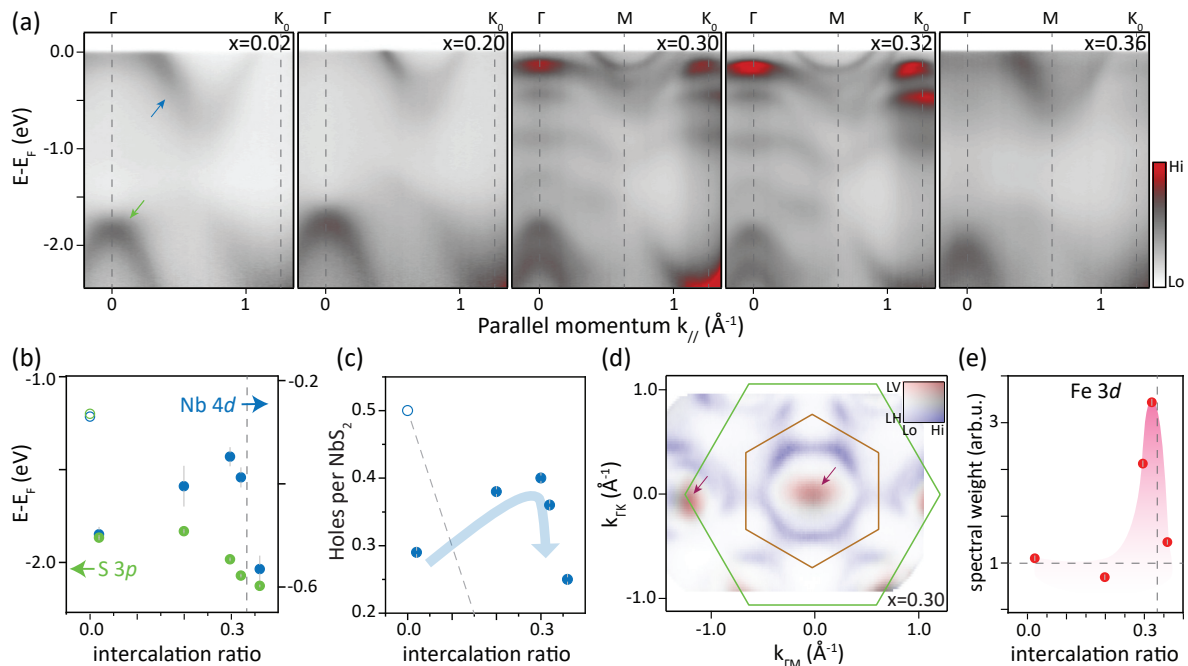


FIG. 2. ARPES measurement of Fe_xNbS_2 across different Fe stoichiometry. (a) Energy-momentum cut along Γ - M - K_0 with different Fe stoichiometry. (b, c) Evolution of the position of S 3p and Nb 4d derived bands and number of holes calculated using Luttinger theorem with increasing Fe stoichiometry. Data for $x = 0$ (hollow points) corresponds to $k_z = 0$ and are extracted from Fig. 1 (c) (DFT calculated band structure) of [36]. (d) Constant energy contours integrated between $E_B = 0.2$ eV and 0.1 eV for $x = 0.30$. Purple arrows indicate Fe-derived bands. Axis labels $k_{\Gamma M}$ and $k_{\Gamma K}$ mark directions to high-symmetry points in the $\text{Fe}_{1/3}\text{NbS}_2$ Brillouin zone. (e) Evolution of spectral weight of the Fe-derived bands with increasing Fe stoichiometry. Spectral weight integrated between $[0,1]$ eV binding energy and $\pm 0.2 \text{ \AA}^{-1}$ of Γ .

This non-monotonic evolution in charge transfer behavior naturally raises the question of where the extra Fe 3d electrons go, which by Hund’s rules carry a net magnetic moment in a high spin state according to prior neutron scattering studies [39]. Strikingly, at $x = 0.30$ and $x = 0.32$ where Nb states receive the least charge doping, a cascade of low-energy, weakly dispersive bands form at Γ , with in-plane bandwidths less than 150 meV. The Fe 3d character of these states are confirmed via Resonant Photoemission Spectroscopy (RPES) measurements at Fe L edge (Fig. S12 [60]). Figure 2 (d) shows the momentum-dependent spectral intensity integrated between $E_B = 0.1$ eV and 0.2 eV where the Fe 3d bands are primarily located. Here, orbital contributions reflected through orthogonal incident photon polarizations are color-coded in red and blue [63]. Via photoemission matrix element analysis (Fig. S4 [60]), these low-energy narrow bands are mainly of $3d_{z^2}$ orbital character [64], and are found to repeat corresponding to the Fe-sublattice Brillouin zone. They belong to the t_{2g} states in the Fe ion’s local symmetry coordinate basis, consistent with our spin-resolved density functional theory (DFT) calculations (Fig. S11 [60]), and are expected to carry local moments despite their very low binding energy — a stark contrast to what is typically observed in other 3d

metal-intercalated TMDs [48, 50, 53, 54, 57, 65, 66]. This not only offers a natural explanation for the “missing electrons” that would have delocalized into the TMD layers, but also hints at potentially fragile magnetism against low-energy chemical, electrical, and temperature tuning.

Given that d_{z^2} orbital is expected to extend along c axis and be the primary orbital to bridge adjacent NbS_2 layers, we turn to investigate their potential role in facilitating c axis itinerancy and indirect Fe-Fe magnetic exchange. Figure 3 shows the energy-momentum cut along Γ - M and A - L directions, as well as the k_z dispersion for Fe 3d and Nb 4d bands. Here, the Fe $3d_{z^2}$ bands show negligible k_z dispersion (Fig. 3(b)(c)), confirming the localized nature of low-energy Fe states along all directions. In contrast, the Nb 4d band gains substantial k_z dispersion on the order of ~ 200 meV compared to mere ~ 35 meV in undoped NbS_2 (extracted from Fig. 1 (c) of [36]).

The enhanced c -axis dispersion of the Nb 4d states signifies strong Fe–Nb hybridization, dominated by a direct σ -overlap between Fe $3d_{z^2}$ and Nb $4d_{z^2}$ orbitals [36], and consistent with their axial alignment along $[001]$. We visualize the energetic consequence

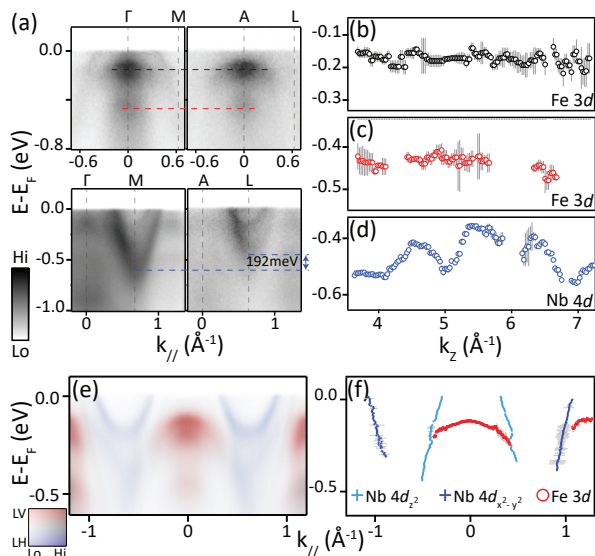


FIG. 3. Mixed dimensionality and hybridization between Fe $3d$ and Nb $4d$ states. (a) Energy-momentum cut along Γ - M - K_0 and A - L - H_0 for $x = 0.30$ collected at LV (upper panel) and LH (lower panel) polarizations, respectively. The black, red and blue dash lines are visual guides to compare band energy positions. (b-d) Scatter points tracking k_z dispersion for Fe-derived bands (black and red circles) and Nb-derived bands (blue circles) extracted from EDC fitting results (Fig. S6). (e) Data reproduced from Fig. 2 (a) on $x = 0.32$, highlighting orbital contributions using a matching color scale to Fig. 2 (d). (f) Fitted trajectory extracted from (e).

of this interaction in Fig. 3(e,f) as a distinctive ‘kink’ in the Nb band at $E_B \approx -0.2$ eV, coinciding with its intersection with the Fe $3d_{2z}$ band. Crucially, this orbital overlap provides the microscopic pathway for strong, itinerant-mediated RKKY exchange [67–69], offering a direct energetic measure of the interaction strength between Fe local moment and NbS₂ itinerant electrons [70–72]. Such three-dimensional connectivity challenges the strict 2D classification often applied to intercalated TMDs [7, 8, 19, 21, 26, 34], distinguishing them from their pristine hosts [2, 4, 36].

Next, to understand the acute transition in charge, magnetic, and transport properties across x_c , we turn to the doping dependent electronic structure. Surprisingly, the low-energy Fe $3d$ states suddenly lose spectral weight above x_c (Fig. 2 (a) and (e), see also Fig. S7 for spectral normalization procedures [60]). Fe site-disorder effect is minimal and smoothly evolves across x_c evidenced by high-resolution synchrotron XRD (Fig. S9 [60]). Furthermore, we explicitly exclude micron-scale surface termination inhomogeneity — previously suggested as a potential confounding factor [55]—through comprehensive micro-XPS (Fig. S2 [60]), real-space micro-ARPES mapping (Fig. S3 [60]), as well as the robust persistence of these phenomena over a wide range

of photon energies probing deeper into the bulk (Fig. 3, Fig. S6). Notably, no discernible Fermi surface folding is seen with the magnetic and charge orders, ruling out a possible low-energy Fermi surface nesting scenario (Fig. S5 [60]) [45].

Taken together, these findings provide compelling evidence that the abrupt electronic reconstruction may originate from a correlation-driven breakdown of the Fe $3d$ quasiparticles (see Fig. S7 (e) for detailed analysis [60]). This sudden decoherence also effectively weakens the c -axis Fe $3d_{2z}$ -Nb $4d_{2z}$ hybridization, suggesting a collapse of the effective c -axis hopping channel $t_{\text{Fe-Nb}}$ above x_c . This in turn leads to a relative reduction of the out-of-plane Heisenberg exchange parameter $|J'_2|$ compared to in-plane parameters. To leading order, such a suppression naturally drives the system from the stripe-ordered ($|J'_2| > |J_2| + 2|J'_3|$) to the zigzag-ordered regime ($|J'_2| < |J_2| + 2|J'_3|$) [Fig. 1 (b)] [39]. This scenario is corroborated by spin-resolved DFT calculations, which show that while increasing the effective Hubbard U parameter, a measure of on-site correlation, suppresses all exchange couplings, it preferentially reduces the ratio $|J'_2|/|J_2|$ to stabilize the zigzag ground state [41]. Interestingly, this mechanism echoes the fragile low-energy hybridization suppressed by the orbital-selective Mott transition (OSMT) of the Fe $3d_{xy}$ band in iron-based superconductors [73–75], where the OSMT strongly reshapes both the local moment and spin density wave tendencies [76, 77]. Here, however, the itinerant carriers originate mainly from TMD orbitals, hence the Hund’s coupling effect on Fe is weak and the dominant source of long-range magnetic exchange is via the Fe–Nb d_{2z} band hybridization.

To understand the electronic structure associated with the stripe and zigzag phases, we perform spin-polarized DFT calculations for stoichiometric Fe_{1/3}NbS₂ with the generalized gradient approximation of Perdew, Burke, and Ernzerhof (PBE) functional [78] and a Hubbard U correction [79] acting on the Fe d electrons. The Vienna Ab initio simulation package (VASP) [80] is used for all calculations; further computational details are provided in SI [60]. Following prior calculations on Fe_{1/3}NbS₂ [39, 41], we employ a U of 0.3 eV for the AFM stripe phase ($x < x_c$) and 0.9 eV ($x > x_c$) for the AFM zigzag phase. These choices lead to computed magnetic moments on the Fe sites of 2.86 and 2.89 μ_B for stripe and zigzag phases, respectively, in agreement with prior reports [30, 39, 81].

Figure 4 (a) plots the computed partial density of states (PDOS) for one of the Fe spin sublattices in the stripe (zigzag) antiferromagnetic phase in the left (right) sub-panel with Nb-projected states overlaid.

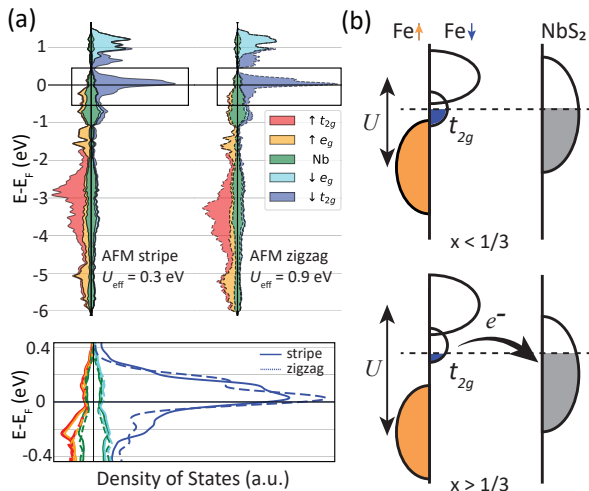


FIG. 4. (a) Projected electronic density of states (DOS) of the Fe spin sublattices in $\text{Fe}_{1/3}\text{NbS}_2$ for AFM stripe (left) and AFM zigzag (right) magnetic phases as computed by DFT. The Fe 3d orbitals are further projected by their t_{2g} and e_g irreducible representation characters as well as their spin channels of spin-up (bonding) and spin-down (anti-bonding) respectively (indicated by different colors). (b) Orbital diagrams depicting the Fe 3d band splitting and occupation below and above the critical doping boundary $x_c = 1/3$.

The pseudo-octahedral coordination about each Fe cation motivates projecting the PDOS onto t_{2g} and e_g 3d molecular orbitals (Fig. S11 [60]), revealing that the strong peak in the DOS near the Fermi level is dominantly of Fe 3d t_{2g} character, corroborating the interpretation of ARPES data near x_c in Fig. 2 (a). The full occupation of the Fe 3d e_g bonding orbitals and the partial filling of the Fe 3d anti-bonding t_{2g} orbitals support a high-spin Fe(II) oxidation state consistent with our computed magnetic moments and prior neutron scattering studies [39]. Further, the bonding Fe e_g 3d states below the Fermi energy divide into two broad levels separated by ~ 2 eV. This subsequent splitting of the occupied e_g level is evidence of a crystal field associated with the Fe site's lower C_{3v} global point group symmetry [82] and reflects significant hybridization of the Fe and Nb states. Strong Fe-Nb hybridization is evident from the greater broadening of the occupied compared to the unoccupied Fe 3d states, and from their energy overlap with the occupied Nb 4d states in the Nb-projected PDOS shown in Fig. 4 (a).

Notably, the partially-occupied t_{2g} states residing at the Fermi energy (E_F) are computed to differ for the two phases, with substantial reorganization of these antibonding 3d states in the zigzag phase relative to stripe. As shown in the zoomed-in view between -400 meV and 400 meV of the PDOS plot in Fig. 4 (a), in the transition from the stripe to the zigzag phase,

this t_{2g} level is pushed above E_F , while the PDOS tail falls 400 meV below E_F , qualitatively consistent with ARPES observation for $x > x_c$ (Fig. 2). More drastic differences in the PDOS of the occupied t_{2g} orbitals further below E_F between the two phases are also observed in our calculations. The schematic in Fig. 4 (b) summarizes the electronic structure evolution across x_c . As x increases above $1/3$, the zigzag phase is favored, where the increased U depopulates these t_{2g} states and causes a decoherence of occupied Fe states above x_c , leading to more electrons returning to the Nb 4d states. This occupation change of Fe t_{2g} states is consistent with the observation in Fig. 2 (b), as well as a slightly enhanced Fe pre- L_3 edge peak for $x = 0.36$ in XAS measurements (Fig. S12 [60]) and the slightly increased ordered moment size due to the removal of anti-bonding Fe electrons for $x > x_c$ seen in neutron scattering [39].

To conclude, by isolating the moment-carrying Fe states near E_F , we have revealed that the sudden collapse of local-itinerant hybridization across x_c dictates the effective exchange J and drives the magnetic phase transition. This correlation-driven electronic reconstruction distinguishes Fe-intercalated TMDs from isostructural systems exhibiting continuous evolution, offering a clear explanation for the sharp phase boundary at $x_c = 1/3$. Methodologically, we demonstrate that ARPES can effectively reveal J_{eff} in metallic magnets by directly visualizing orbital-specific hybridization. Looking forward, atomically resolved probes such as scanning tunneling microscope/spectroscopy (STM/S), and surface-specific magnetic probes such as XPEEM, may help shed light on the atomic origin of the sudden change in the correlation strength in Fe across x_c , potentially by mapping local Fe vacancy or interstitial disorders to specific magnetization states.

ACKNOWLEDGMENTS

We thank Eduardo H. da Silva Neto, Pranab Kumar-Nag, Xinze Yang, Sophie Weber, Tianyu Zhu, Ke Liao, Ming Yi, and Ruihua He for helpful discussions. Work at Yale University was funded by the U.S. Air Force Office of Scientific Research under Award No. FA9550-24-1-0048. W. L. acknowledges support from James Kouvel Fellowship. Work at the University of California, Berkeley and Lawrence Berkeley National Laboratory was funded by the U.S. DOE, Office of Science, Office of Basic Energy Sciences, Materials Sciences and Engineering Division under Contract No. DE-AC02-05CH11231 (Quantum Materials Program KC2202). DFT calculations were computed using the NERSC supercomputing resources at Lawrence Berkeley National Lab under the Theory of Materials FWP program. Work at the University of California, San

Diego was supported by the National Science Foundation under Grant No. DMR-2145080. Bulk crystal growth of NbS₂ materials was supported by the 2DCC-MIP under NSF cooperative agreement DMR-2039351. Use of the Stanford Synchrotron Radiation Lightsource, SLAC National Accelerator Laboratory, is supported by the U.S. Department of Energy, Office of Science, Office of Basic Energy Sciences under Contract No. DE-AC02-76SF00515. This research used resources of the National Synchrotron Light Source II, operated under Contract No. DE-SC0012704. The authors also acknowledge the Brookhaven National Laboratory-Yale partner user agreement PU-313536. We acknowledge Yale West Campus Materials Characterization Core. This work is based on research conducted at the Center for High-Energy X-ray Sciences (CHEXS), which is supported by the National Science Foundation (BIO, ENG and MPS Directorates) under award DMR-2342336. This research used resources of the Advanced Light Source, a US DOE Office of Science User Facility under Contract No. DE-AC02-05CH11231. This research used resources of the Advanced Photon Source, a U.S. Department of Energy (DOE) Office of Science User Facility operated for the DOE Office of Science by Argonne National Laboratory under Contract No. DE-AC02-06CH11357.

* yu.he@yale.edu

- [1] J. Wilson, F. D. Salvo, and S. Mahajan, Charge-density waves and superlattices in the metallic layered transition metal dichalcogenides, *Advances in Physics* **24**, 117 (1975).
- [2] S. V. Borisenko, A. A. Kordyuk, V. B. Zabolotnyy, D. S. Inosov, D. Evtushinsky, B. Büchner, A. N. Yaresko, A. Varykhalov, R. Follath, W. Eberhardt, L. Patthey, and H. Berger, Two Energy Gaps and Fermi-Surface “Arcs” in NbSe₂, *Phys. Rev. Lett.* **102**, 166402 (2009).
- [3] T. Valla, A. V. Fedorov, P. D. Johnson, P.-A. Glans, C. McGuinness, K. E. Smith, E. Y. Andrei, and H. Berger, Quasiparticle Spectra, Charge-Density Waves, Superconductivity, and Electron-Phonon Coupling in 2H-NbSe₂, *Phys. Rev. Lett.* **92**, 086401 (2004).
- [4] D. J. Rahn, S. Hellmann, M. Kalläne, C. Sohr, T. K. Kim, L. Kipp, and K. Rossnagel, Gaps and kinks in the electronic structure of the superconductor 2H-NbSe₂ from angle-resolved photoemission at 1 K, *Phys. Rev. B* **85**, 224532 (2012).
- [5] S. Manzeli, D. Ovchinnikov, D. Pasquier, O. V. Yazyev, and A. Kis, 2d transition metal dichalcogenides, *Nature Reviews Materials* **2**, 17033 (2017).
- [6] W. Choi, N. Choudhary, G. H. Han, J. Park, D. Akinwande, and Y. H. Lee, Recent development of two-dimensional transition metal dichalcogenides and their applications, *Materials Today* **20**, 116 (2017).
- [7] S. S. P. Parkin and R. H. Friend, 3d transition-metal intercalates of the niobium and tantalum dichalcogenides. i. magnetic properties, *Philosophical Magazine B* **41**, 65 (1980).
- [8] R. H. Friend, A. R. Beal, and A. D. Yoffe, Electrical and magnetic properties of some first row transition metal intercalates of niobium disulphide, *The Philosophical Magazine: A Journal of Theoretical Experimental and Applied Physics* **35**, 1269 (1977).
- [9] F. W. Boswell, A. Prodan, W. R. Vaughan, and J. M. Corbett, On the ordering of Fe atoms in Fe_xNbS₂, *physica status solidi (a)* **45**, 469 (1978).
- [10] Y. Togawa, T. Koyama, K. Takayanagi, S. Mori, Y. Kousaka, J. Akimitsu, S. Nishihara, K. Inoue, A. S. Ovchinnikov, and J. Kishine, Chiral magnetic soliton lattice on a chiral helimagnet, *Phys. Rev. Lett.* **108**, 107202 (2012).
- [11] D. Braam, C. Gomez, S. Tezok, E. V. L. de Mello, L. Li, D. Mandrus, H.-Y. Kee, and J. E. Sonier, Magnetic properties of the helimagnet Cr_{1/3}NbS₂ observed by μ SR, *Phys. Rev. B* **91**, 144407 (2015).
- [12] Y. Kousaka, T. Ogura, J. Zhang, P. Miao, S. Lee, S. Torii, T. Kamiyama, J. Campo, K. Inoue, and J. Akimitsu, Long Periodic Helimagnetic Ordering in CrM₃S₆ (M = Nb and Ta), *Journal of Physics: Conference Series* **746**, 012061 (2016).
- [13] Y. Kousaka, Y. Nakao, J. Kishine, M. Akita, K. Inoue, and J. Akimitsu, Chiral helimagnetism in T_{1/3}NbS₂ (T=Cr and Mn), *Nuclear Instruments and Methods in Physics Research Section A: Accelerators, Spectrometers, Detectors and Associated Equipment* **600**, 250 (2009).
- [14] S. K. Karna, F. N. Womack, R. Chapai, D. P. Young, M. Marshall, W. Xie, D. Graf, Y. Wu, H. Cao, L. DeBeer-Schmitt, P. W. Adams, R. Jin, and J. F. DiTusa, Consequences of magnetic ordering in chiral Mn_{1/3}NbS₂, *Phys. Rev. B* **100**, 184413 (2019).
- [15] Y. Togawa, T. Koyama, Y. Nishimori, Y. Matsumoto, S. McVitie, D. McGrouther, R. L. Stamps, Y. Kousaka, J. Akimitsu, S. Nishihara, K. Inoue, I. G. Bostrem, V. E. Sinitsyn, A. S. Ovchinnikov, and J. Kishine, Magnetic soliton confinement and discretization effects arising from macroscopic coherence in a chiral spin soliton lattice, *Phys. Rev. B* **92**, 220412 (2015).
- [16] N. J. Ghimire, A. S. Botana, J. S. Jiang, J. Zhang, Y. S. Chen, and J. F. Mitchell, Large anomalous Hall effect in the chiral-lattice antiferromagnet CoNb₃S₆, *Nature Communications* **9**, 3280 (2018).
- [17] R. Aoki, Y. Kousaka, and Y. Togawa, Anomalous nonreciprocal electrical transport on chiral magnetic order, *Phys. Rev. Lett.* **122**, 057206 (2019).
- [18] P. Park, Y.-G. Kang, J. Kim, K. H. Lee, H.-J. Noh, M. J. Han, and J.-G. Park, Field-tunable toroidal moment and anomalous Hall effect in noncollinear antiferromagnetic Weyl semimetal Co_{1/3}TaS₂, *npj Quantum Materials* **7**, 42 (2022).
- [19] J. van den Berg and P. Cossee, Structural aspects and magnetic behaviour of NbS₂ and TaS₂ containing extra metal atoms of the first transition series, *Inorganica Chimica Acta* **2**, 143 (1968).
- [20] F. Hulliger and E. Pobitschka, On the magnetic behavior of new 2H-NbS₂-type derivatives, *Journal of Solid State Chemistry* **1**, 117 (1970).
- [21] B. Van Laar, H. Rietveld, and D. Ijdo, Magnetic and crystallographic structures of Me_xNbS₂ and Me_xTaS₂, *Journal of Solid State Chemistry* **3**, 154 (1971).
- [22] M. Eibschütz, F. J. DiSalvo, J. Hull, G. W., and S. Mahajan, Ferromagnetism in metallic Fe_xTaS₂

- ($x \approx 0.28$), *Applied Physics Letters* **27**, 464 (1975).
- [23] A. L. Blanc-Soreau, J. Rouxel, M.-F. Gardette, and O. Gorochov, Propriétés électriques et magnétiques de $\text{Mn}_{0.25}\text{NbS}_2$ et $\text{Mn}_{0.33}\text{NbS}_2$, *Materials Research Bulletin* **11**, 1061 (1976).
- [24] H. Wang, X.-P. Ma, X.-Y. Zeng, J. Gong, J.-F. Lin, X.-Y. Wang, Z.-Y. Dai, K. Han, Y.-T. Wang, and T.-L. Xia, Anomalous Hall effect and topological Hall effect in the noncollinear antiferromagnet $\text{V}_{0.3}\text{NbS}_2$, *Phys. Rev. B* **107**, 134436 (2023).
- [25] T. Inoshita, M. Hirayama, N. Hamada, H. Hosono, and S. Murakami, Topological semimetal phases manifested in transition metal dichalcogenides intercalated with 3d metals, *Phys. Rev. B* **100**, 121112 (2019).
- [26] Y. Yamasaki, R. Moriya, M. Arai, S. Masubuchi, S. Pyon, T. Tamegai, K. Ueno, and T. Machida, Exfoliation and van der Waals heterostructure assembly of intercalated ferromagnet $\text{Cr}_{1/3}\text{TaS}_2$, *2D Materials* **4**, 041007 (2017).
- [27] A. F. Gubkin, E. P. Proskurina, Y. Kousaka, E. M. Sherokalova, N. V. Selezneva, P. Miao, S. Lee, J. Zhang, Y. Ishikawa, S. Torii, T. Kamiyama, J. Campo, J. Akimitsu, and N. V. Baranov, Crystal and magnetic structures of $\text{Cr}_{1/3}\text{NbSe}_2$ from neutron diffraction, *Journal of Applied Physics* **119**, 013903 (2016).
- [28] N. Toporova, E. Sherokalova, N. Selezneva, V. Ogloblichev, and N. Baranov, Crystal structure, properties and griffiths-like phase in niobium diselenide intercalated with chromium, *Journal of Alloys and Compounds* **848**, 156534 (2020).
- [29] H. Zhang, W. Wei, G. Zheng, J. Lu, M. Wu, X. Zhu, J. Tang, W. Ning, Y. Han, L. Ling, J. Yang, W. Gao, Y. Qin, and M. Tian, Electrical and anisotropic magnetic properties in layered $\text{Mn}_{1/3}\text{TaS}_2$ crystals, *Applied Physics Letters* **113**, 072402 (2018).
- [30] P. Liu, H. Zhu, Q. Wu, Y. Lu, and Y. Pu, Unconventional magneto-transport properties of the layered antiferromagnet $\text{Fe}_{1/3}\text{NbS}_2$, *Applied Physics Letters* **121**, 081901 (2022).
- [31] S. Mangelsen, J. Hansen, P. Adler, W. Schnelle, W. Bensch, S. Mankovsky, S. Polesya, and H. Ebert, Large Anomalous Hall Effect and Slow Relaxation of the Magnetization in $\text{Fe}_{1/3}\text{TaS}_2$, *The Journal of Physical Chemistry C* **124**, 24984 (2020).
- [32] J. Dijkstra, P. J. Zijlema, C. F. van Bruggen, C. Haas, and R. A. de Groot, Band-structure calculations of $\text{Fe}_{1/3}\text{TaS}_2$ and $\text{Mn}_{1/3}\text{TaS}_2$, and transport and magnetic properties of $\text{Fe}_{0.28}\text{TaS}_2$, *Journal of Physics: Condensed Matter* **1**, 6363 (1989).
- [33] K. Lu, A. Murzabekova, S. Shim, J. Park, S. Kim, L. Kish, Y. Wu, L. DeBeer-Schmitt, A. A. Aczel, A. Schleife, N. Mason, F. Mahmood, and G. J. MacDougall, Understanding the Anomalous Hall effect in $\text{Co}_{1/3}\text{NbS}_2$ from crystal and magnetic structures (2022), [arXiv:2212.14762](https://arxiv.org/abs/2212.14762).
- [34] Y. Liu, Z. Hu, X. Tong, E. D. Bauer, and C. Petrovic, Electrical and thermal transport in van der Waals magnets $2\text{H}-\text{M}_x\text{TaS}_2$ ($\text{M} = \text{Mn}, \text{Co}$), *Phys. Rev. Res.* **4**, 013048 (2022).
- [35] Y. An, P. Park, C. Kim, K. Zhang, H. Kim, M. Avdeev, J. Kim, M.-J. Han, H.-J. Noh, S. Seong, J.-S. Kang, H.-D. Kim, and J.-G. Park, Bulk properties of the chiral metallic triangular antiferromagnets $\text{Ni}_{1/3}\text{NbS}_2$ and $\text{Ni}_{1/3}\text{TaS}_2$, *Phys. Rev. B* **108**, 054418 (2023).
- [36] Z. El Youbi, S. W. Jung, C. Richter, K. Hricovini, C. Cacho, and M. D. Watson, Fermiology and electron-phonon coupling in the 2H and 3R polytypes of NbS_2 , *Phys. Rev. B* **103**, 155105 (2021).
- [37] L. Šmejkal, J. Sinova, and T. Jungwirth, Beyond conventional ferromagnetism and antiferromagnetism: A phase with nonrelativistic spin and crystal rotation symmetry, *Phys. Rev. X* **12**, 031042 (2022).
- [38] L. Šmejkal, J. Sinova, and T. Jungwirth, Emerging research landscape of altermagnetism, *Phys. Rev. X* **12**, 040501 (2022).
- [39] S. Wu, Z. Xu, S. C. Haley, S. F. Weber, A. Acharya, E. Maniv, Y. Qiu, A. A. Aczel, N. S. Settineri, J. B. Neaton, J. G. Analytis, and R. J. Birgeneau, Highly Tunable Magnetic Phases in Transition-Metal Dichalcogenide $\text{Fe}_{1/3+\delta}\text{NbS}_2$, *Phys. Rev. X* **12**, 021003 (2022).
- [40] N. P. Bentley, T. L. Breeze, A. Hernández-Melián, T. J. Hicken, B. M. Huddart, F. L. Pratt, A. E. Hall, D. A. Mayoh, G. Balakrishnan, S. J. Clark, and T. Lancaster, Magnetism in $\text{M}_{1/3}\text{NbS}_2$ ($\text{M} = \text{Fe}, \text{V}, \text{Mn}$): Insight into intercalated transition metal dichalcogenides using μSR , *Phys. Rev. B* **112**, 134453 (2025).
- [41] S. F. Weber and J. B. Neaton, Origins of anisotropic transport in the electrically switchable antiferromagnet $\text{Fe}_{1/3}\text{NbS}_2$, *Phys. Rev. B* **103**, 214439 (2021).
- [42] N. L. Nair, E. Maniv, C. John, S. Doyle, J. Orenstein, and J. G. Analytis, Electrical switching in a magnetically intercalated transition metal dichalcogenide, *Nature Materials* **19**, 153 (2020).
- [43] E. Maniv, R. A. Murphy, S. C. Haley, S. Doyle, C. John, A. Maniv, S. K. Ramakrishna, Y.-L. Tang, P. Ercius, R. Ramesh, A. P. Reyes, J. R. Long, and J. G. Analytis, Exchange bias due to coupling between coexisting antiferromagnetic and spin-glass orders, *Nature Physics* **10.1038/s41567-020-01123-w** (2021).
- [44] E. Maniv, N. L. Nair, S. C. Haley, S. Doyle, C. John, S. Cabrini, A. Maniv, S. K. Ramakrishna, Y.-L. Tang, P. Ercius, R. Ramesh, Y. Tserkovnyak, A. P. Reyes, and J. G. Analytis, Antiferromagnetic switching driven by the collective dynamics of a coexisting spin glass, *Science Advances* **7**, 10.1126/sciadv.abd8452 (2021).
- [45] S. Wu, R. Basak, W. Li, J.-W. Kim, P. J. Ryan, D. Lu, M. Hashimoto, C. Nelson, R. Acevedo-Esteves, S. C. Haley, J. G. Analytis, Y. He, A. Frano, and R. J. Birgeneau, Discovery of Charge Order in the Transition Metal Dichalcogenide Fe_xNbS_2 , *Phys. Rev. Lett.* **131**, 186701 (2023).
- [46] Z. Hawkhead, T. J. Hicken, N. P. Bentley, B. M. Huddart, S. J. Clark, and T. Lancaster, Band-filling-controlled magnetism from transition metal intercalation in $\text{N}_{1/3}\text{NbS}_2$ revealed with first-principles calculations, *Phys. Rev. Mater.* **7**, 114002 (2023).
- [47] C. Battaglia, H. Cercellier, L. Despont, C. Monney, M. Prester, H. Berger, L. Forró, M. G. Garnier, and P. Aebi, Non-uniform doping across the Fermi surface of NbS_2 intercalates, *The European Physical Journal B* **57**, 385 (2007).
- [48] P. Popčević, Y. Utsumi, I. Biało, W. Tabis, M. A. Gala, M. Rosmus, J. J. Kolodziej, N. Tomaszewska, M. Garb, H. Berger, I. Batistić, N. Barišić, L. Forró, and E. Tutiš, Role of intercalated cobalt in the electronic structure of $\text{Co}_{1/3}\text{NbS}_2$, *Phys. Rev. B* **105**, 155114 (2022).

- [49] N. Qin, C. Chen, S. Du, X. Du, X. Zhang, Z. Yin, J. Zhou, R. Xu, X. Gu, Q. Zhang, W. Zhao, Y. Li, S.-K. Mo, Z. Liu, S. Zhang, Y. Guo, P. Tang, Y. Chen, and L. Yang, Persistent exchange splitting in the chiral helimagnet $\text{Cr}_{1/3}\text{NbS}_2$, *Phys. Rev. B* **106**, 035129 (2022).
- [50] N. Sirica, S.-K. Mo, F. Bondino, I. Pis, S. Nappini, P. Vilmercati, J. Yi, Z. Gai, P. C. Snijders, P. K. Das, I. Vobornik, N. Ghimire, M. R. Koehler, L. Li, D. Sapkota, D. S. Parker, D. G. Mandrus, and N. Mannella, Electronic structure of the chiral helimagnet and $3d$ -intercalated transition metal dichalcogenide $\text{Cr}_{1/3}\text{NbS}_2$, *Phys. Rev. B* **94**, 075141 (2016).
- [51] L. S. Xie, O. Gonzalez, K. Li, M. Michiardi, S. Gorovikov, S. H. Ryu, S. S. Fender, M. Zonno, N. H. Jo, S. Zhdanovich, C. Jozwiak, A. Bostwick, S. Husremović, M. P. Erodici, C. Mollazadeh, A. Damascelli, E. Rotenberg, Y. Ping, and D. K. Bediako, Comparative Electronic Structures of the Chiral Helimagnets $\text{Cr}_{1/3}\text{NbS}_2$ and $\text{Cr}_{1/3}\text{TaS}_2$, *Chemistry of Materials* **35**, 7239 (2023).
- [52] B. Edwards, O. Downton, A. E. Hall, P. A. E. Murgatroyd, S. Buchberger, T. Antonelli, G.-R. Siemann, A. Rajan, E. A. Morales, A. Zivanovic, C. Bigi, R. V. Belosludov, C. M. Polley, D. Carbone, D. A. Mayoh, G. Balakrishnan, M. S. Bahramy, and P. D. C. King, Giant valley-zeeman coupling in the surface layer of an intercalated transition metal dichalcogenide, *Nature Materials* **22**, 459 (2023).
- [53] Y. U. Boucher, I. Bialo, M. A. Gala, W. Tabiś, M. Rosmus, N. Olszowska, J. J. Kolodziej, B. Gudac, M. Novak, N. K. C. Muniraju, I. Batistić, N. Barišić, P. Popčević, and E. Tutiš, *Intercalation-induced states at the Fermi level and the coupling of intercalated magnetic ions to conducting layers in $\text{Ni}_{1/3}\text{NbS}_2$* (2024), [arXiv:2401.05884 \[cond-mat.mtrl-sci\]](https://arxiv.org/abs/2401.05884).
- [54] A. Kar, R. Basak, X. Li, A. Korshunov, D. Subires, J. Phillips, C. Y. Lim, F. Zhou, L. Song, W. Wang, Y.-C. Lau, G. Garbarino, P. Gargiani, Y. Zhao, C. Plueckthun, S. Francoual, A. Jana, I. Vobornik, T. Valla, A. Rajapitamahuni, J. G. Analytis, R. J. Birgeneau, E. Vescovo, A. Bosak, J. Dai, M. Tallarida, A. Frano, V. Pardo, S. Wu, and S. Blanco-Canosa, *Magnetoelastic coupling in intercalated transition metal dichalcogenides* (2025), [arXiv:2503.14444 \[cond-mat.str-el\]](https://arxiv.org/abs/2503.14444).
- [55] B. Edwards, D.-A. Deaconu, P. A. E. Murgatroyd, S. Buchberger, T. Antonelli, D. Halliday, G.-R. Siemann, A. Zivanovic, L. Trzaska, A. Rajan, E. Abarca Morales, D. A. Mayoh, A. E. Hall, R. V. Belosludov, M. D. Watson, T. K. Kim, D. Biswas, T.-L. Lee, C. M. Polley, D. Carbone, M. Leandersson, G. Balakrishnan, M. S. Bahramy, and P. D. C. King, Chemical trends of the bulk and surface termination-dependent electronic structure of metal-intercalated transition metal dichalcogenides, *Chemistry of Materials* **36**, 7117 (2024).
- [56] H. Tanaka, S. Okazaki, K. Kuroda, R. Noguchi, Y. Arai, S. Minami, S. Ideta, K. Tanaka, D. Lu, M. Hashimoto, V. Kandyba, M. Cattelan, A. Barinov, T. Muro, T. Sasagawa, and T. Kondo, Large anomalous Hall effect induced by weak ferromagnetism in the noncentrosymmetric antiferromagnet CoNb_3S_6 , *Phys. Rev. B* **105**, L121102 (2022).
- [57] H. Tian, T. Li, Y. Zhang, Y. Li, Z. Shen, Y. Wu, Z. Wei, Y. Chu, W. Lan, X. Zheng, Z. Shang, Z. Wang, P. Wu, G. Gao, M. Ge, Y. Wang, M. Shi, Z. Liu, L. Zhang, D. Shen, Y. Liu, Z. Wang, Z. Liu, S. Cui, L. Song, and Z. Sun, 2×2 Charge Density Wave in $\text{Fe}_{0.33}\text{NbSe}_2$ Stabilized by Disordered Intercalation, *ACS Nano* **19**, 31340 (2025), PMID: 40845329.
- [58] A. Damascelli, Z. Hussain, and Z.-X. Shen, Angle-resolved photoemission studies of the cuprate superconductors, *Rev. Mod. Phys.* **75**, 473 (2003).
- [59] J. A. Sobota, Y. He, and Z.-X. Shen, Angle-resolved photoemission studies of quantum materials, *Rev. Mod. Phys.* **93**, 025006 (2021).
- [60] See Supplemental Material for details on experimental and computational methods, analysis on X-ray photoelectron spectroscopy (XPS), single crystal X-ray diffraction (XRD) and X-ray absorption spectroscopy (XAS) results, and additional data and analysis from ARPES measurements and DFT calculations.
- [61] J. M. Luttinger, Fermi surface and some simple equilibrium properties of a system of interacting fermions, *Phys. Rev.* **119**, 1153 (1960).
- [62] C. Heil, M. Schlipf, and F. Giustino, Quasiparticle *GW* band structures and Fermi surfaces of bulk and monolayer NbS_2 , *Phys. Rev. B* **98**, 075120 (2018).
- [63] C. Jozwiak, J. A. Sobota, K. Gotlieb, A. F. Kemper, C. R. Rotundu, R. J. Birgeneau, Z. Hussain, D.-H. Lee, Z.-X. Shen, and A. Lanzara, Spin-polarized surface resonances accompanying topological surface state formation, *Nature Communications* **7**, 13143 (2016).
- [64] S. Moser, An experimentalist's guide to the matrix element in angle resolved photoemission, *Journal of Electron Spectroscopy and Related Phenomena* **214**, 29 (2017).
- [65] H. Park and I. Martin, DFT + DMFT study of the magnetic susceptibility and the correlated electronic structure in transition-metal intercalated NbS_2 , *Phys. Rev. B* **109**, 085110 (2024).
- [66] S. Mankovsky, S. Polesya, H. Ebert, and W. Bensch, Electronic and magnetic properties of $2H - \text{NbS}_2$ intercalated by $3d$ transition metals, *Phys. Rev. B* **94**, 184430 (2016).
- [67] D. N. Aristov, Indirect RKKY interaction in any dimensionality, *Phys. Rev. B* **55**, 8064 (1997).
- [68] K.-T. Ko, K. Kim, S. B. Kim, H.-D. Kim, J.-Y. Kim, B. I. Min, J.-H. Park, F.-H. Chang, H.-J. Lin, A. Tanaka, and S.-W. Cheong, RKKY Ferromagnetism with Ising-Like Spin States in Intercalated $\text{Fe}_{1/4}\text{TaS}_2$, *Phys. Rev. Lett.* **107**, 247201 (2011).
- [69] M. A. Ruderman and C. Kittel, Indirect exchange coupling of nuclear magnetic moments by conduction electrons, *Phys. Rev.* **96**, 99 (1954).
- [70] S. Kirchner, S. Paschen, Q. Chen, S. Wirth, D. Feng, J. D. Thompson, and Q. Si, Colloquium: Heavy-electron quantum criticality and single-particle spectroscopy, *Rev. Mod. Phys.* **92**, 011002 (2020).
- [71] P. Gegenwart, Q. Si, and F. Steglich, Quantum criticality in heavy-fermion metals, *Nature Physics* **4**, 186 (2008).
- [72] H. Prüser, P. E. Dargel, M. Bouhassoune, R. G. Ulbrich, T. Pruschke, S. Lounis, and M. Wenderoth, Interplay between the Kondo effect and the Ruderman-Kittel-Kasuya-Yosida interaction, *Nature Communications* **5**, 5417 (2014).
- [73] M. Yi, Z.-K. Liu, Y. Zhang, R. Yu, J.-X. Zhu, J. J. Lee, R. G. Moore, F. T. Schmitt, W. Li, S. C. Riggs,

- J.-H. Chu, B. Lv, J. Hu, M. Hashimoto, S.-K. Mo, Z. Hussain, Z. Q. Mao, C. W. Chu, I. R. Fisher, Q. Si, Z.-X. Shen, and D. H. Lu, Observation of universal strong orbital-dependent correlation effects in iron chalcogenides, *Nature Communications* **6**, 7777 (2015).
- [74] M. Yi, H. Pfau, Y. Zhang, Y. He, H. Wu, T. Chen, Z. R. Ye, M. Hashimoto, R. Yu, Q. Si, D.-H. Lee, P. Dai, Z.-X. Shen, D. H. Lu, and R. J. Birgeneau, Nematic Energy Scale and the Missing Electron Pocket in FeSe, *Phys. Rev. X* **9**, 041049 (2019).
- [75] M. Yi, Y. Zhang, Z.-X. Shen, and D. Lu, Role of the orbital degree of freedom in iron-based superconductors, *npj Quantum Materials* **2**, 57 (2017).
- [76] R. Yu and Q. Si, Orbital-Selective Mott Phase in Multiorbital Models for Alkaline Iron Selenides $\mathbf{K}_{1-x}\text{Fe}_{2-y}\text{Se}_2$, *Phys. Rev. Lett.* **110**, 146402 (2013).
- [77] L. de' Medici, S. R. Hassan, M. Capone, and X. Dai, Orbital-Selective Mott Transition out of Band Degeneracy Lifting, *Phys. Rev. Lett.* **102**, 126401 (2009).
- [78] J. P. Perdew, K. Burke, and M. Ernzerhof, Generalized gradient approximation made simple, *Phys. Rev. Lett.* **77**, 3865 (1996).
- [79] A. I. Liechtenstein, V. I. Anisimov, and J. Zaanen, Density-functional theory and strong interactions: Orbital ordering in mott-hubbard insulators, *Phys. Rev. B* **52**, R5467 (1995).
- [80] G. Kresse and J. Furthmüller, Efficient iterative schemes for *ab initio* total-energy calculations using a plane-wave basis set, *Phys. Rev. B* **54**, 11169 (1996).
- [81] Y. Saitoh, K. Kobayashi, A. Fujimori, Y. Yamamura, M. Koyano, T. Tsuji, and S. Katayama, Photoemission and core-level absorption spectroscopy of Fe_xNbS_2 , *Journal of Electron Spectroscopy and Related Phenomena* **144-147**, 829 (2005), proceeding of the Fourteenth International Conference on Vacuum Ultraviolet Radiation Physics.
- [82] L. S. Xie, S. Husremović, O. Gonzalez, I. M. Craig, and D. K. Bediako, Structure and magnetism of iron- and chromium-intercalated niobium and tantalum disulfides, *Journal of the American Chemical Society* **144**, 9525 (2022), pMID: 35584537.